International Journal of Environmental Sciences
ISSN: 2229-7359
Vol. 11 No. 21s, 2025
https://theaspd.com/index.php

Facile Co-Precipitation Synthesis And Multifunctional Properties Of Ni-Doped $Znfe_2O_4$ Nanoparticles

Jaba Sherin. S[1], Maria Lenin.M[2,5], S.R. Gibin[3], R. Gopalakrishnan[4]
[1]Research Scholar, Department of Physics, Annai Velankanni College, Tholayavattam, Kanyakumari District -629157, Tamil Nadu, India.
[2]Associate Professor, Department of Physics, Annai Velankanni College, Tholayavattam, Kanyakumari District – 629157, Tamil Nadu, India
[3]Associate Professor of Physics, Sree Sakthi Engineering College (Autonomous), Karamadai, Coimbatore-641104, Tamil Nadu, India
[4]Assistant Professor of Physics, Sri Ranganathar Institute of engineering and technology Coimbatore - 641110, Tamil Nadu, India
[5]Manonmaniam Sundaranar University, Abishekapatti-627012, Tirunelveli, Tamil Nadu, India.
*Corresponding author: Dr. Maria Lenin.M (E-mail: ria.lenin@gmail.com)

Abstract
In this work, Ni-doped $ZnFe_2O_4$ nanoparticles were prepared by low-cost co-precipitation method. The effects of Ni doping on the phase composition, microstructure, thermal, and electro-chemical properties of $ZnFe_2O_4$ were investigated. X-ray diffraction patterns confirm single-phase cubic spinel structures with crystallite size in the range around 34 nm. Particle sizes obtained from transmission electron micrographs were also in good agreement with the crystallite sizes obtained from the XRD data. FTIR result reveals that the synthesized Ni doped $ZnFe_2O_4$ nanoparticles were of phase pure with cubic structure. EDX image confirm the presence of Ni, Fe, Zn and O in the Ni doped $ZnFe_2O_4$ nanoparticles. Thermo gravimetric and differential thermal analysis (TG/DTA) method was used to confirm the formation of Ni doped $ZnFe_2O_4$ nanoparticles. From the CV analysis, higher capacitance value observed for the scanning rate 2 mV/s. The electrochemical results show that Ni doped $ZnFe_2O_4$ nanoparticles may function well as supercapacitor electrodes. For the sake of designing and optimizing supercapacitors to satisfy future energy needs, this work adds to our knowledge of their electrochemical characteristics and energy storage capacity.
Keywords: *Nanoparticles, Co-precipitation technique, Cubic structure, Thermal, Supercapacitor.*

1. INTRODUCTION

In the recent past the research interests in nano crystalline materials have grown considerably increased because of their large novel physical aspects. These aspects make them very attractive for a variety of applications including but not limited to use as electrodes in energy storage devices, as catalysts, in magnetic storage devices, etc. [1-3]. Now a day, the environmental issues are the most important problem worldwide, and for that reason, there is an important demand for clean, efficient, and sustainable sources of energy as well as efficient technologies for energy storage [2]. With this purpose in mind, iron oxides have been identified as a low-cost and potentially environmentally friendly material. Supercapacitor is much more attractive because it could provide high-power density, high-rate capability, and long cycle life. Even though, greater capacitance and long cycle life is provided by other materials, ferrite-based supercapacitors gained attention due to its non-toxicity and cheaper costs [3]. Spinel ferrite is particularly appealing for spintronic device engineering, energy storage, photo-electrochemical water splitting, and optoelectronic and biomedical applications because its semiconducting and magnetic properties can be tailored by varying the type and concentration of intrinsic defects [4]. In literature, Spinel ferrites have the general formula of AFe_2O_4 (where A^{2+}: Co^{2+}, Ni^{2+}, Mg^{2+}, Zn^{2+} and Mn^{2+}) [5-10] and unit cell contains 32 oxygen atoms in cubic close packing with 8 tetrahedral (Td) and 16 octahedral (Oh) occupied sites. By changing type of the divalent cation, it is possible to obtain significantly different physical and electrical properties in these ferrites. Among the divalent metal ions, zinc improves the efficiency of ferrites in many field especially electrical storage system and photocatalysis [8-13]. Zinc ferrite is a ceramic material that mixes and fires iron (III) oxide with zinc oxide. The $ZnFe_2O_4$ crystallizes in a standard spinel configuration, with Fe and Zn cations distributed among the fcc anion lattice's octahedral and tetrahedral interstitial sites, reported by S. Nadaf et al., [14]. Especially, ferrite family member of zinc ferrite ($ZnFe_2O_4$) exhibits promising potential for the application of supercapacitor, due to abundant resources, low cost, environmental friendliness and high electrochemical activity [15]. However, the $ZnFe_2O_4$ based electrode often suffers from low conductivity, leading to unsatisfactory rate capability [16]. Furthermore, the

morphology and size of the electrode materials also play important roles in determining the performance of supercapacitors [17]. Doping is the critical process that monitors the properties of nanostructured ferrites and obtains new technologically relevant materials that are significant. The optical, electrical and supercapacitor properties of zinc ferrites can be modified strongly by doping systems, the highly abundant electron states make nickel (Ni) as a promising dopant [1]. Ni–Zn ferrite is a mixed spinel in which T_d sites are occupied by Zn^{2+} and Fe^{3+} ions and the O_h sites are occupied by Ni^{2+} and Fe^{3+} in the lattice [18]. The distribution of various ions in T_d and O_h sites is different when the ferrite is synthesized at low temperatures and the particle size is in nanometer region [19]. Further, as per the author's knowledge, there were no previous reports on thermal and electrochemical properties of Ni-doped $ZnFe_2O_4$ nanoparticles prepared by Co-precipitation technique. In order to explain, predict and optimize the properties of Ni-doped $ZnFe_2O_4$ nanoparticles, it is necessary to understand the nature of the electronic properties of Ni-doped $ZnFe_2O_4$ nanoparticles. This paper is aimed at this problem. The Ni-doped $ZnFe_2O_4$ nanoparticles is prepared by Co-precipitation technique. The effect of nickel on the structural, thermal and electrochemical properties of $ZnFe_2O_4$ is systematically studied. The combination of experimental results provides important information for future doping research and supercapacitor applications reference.

2. Experimental

2.1 Synthesis of Ni doped $ZnFe_2O_4$ nanoparticles

The precursor for the formation of Ni doped $ZnFe_2O_4$ nanoparticles was prepared through a novel co-precipitation process, using Ni doped $ZnFe_2O_4$ as the precipitant. All chemicals were sourced from Merck Chemicals. Firstly, $Zn(NO_3)^2{\cdot}6H_2O$, $Fe(NO_3)^2{\cdot}9H_2O$, nickel nitrate hexahydrate ($Ni(NO_3)_2$. $6H_2O$) and citric acid ($C_6H_8O_7$) were separately dissolved in 20 ml of deionized water. Sodium hydroxide (NaOH) was slowly added drop by drop to the mixture, which was stirred at 60 minutes for 80 ◦C. The presence of citric acid behaved as a chelating agent during the process, resulting in the development of brown-colored precipitates. The precipitates were widely cleaned multiple times using deionized water and acetone. Subsequently, they were dried at 80 ◦C to obtain dark brown precipitates. Finally, the precipitates were subjected to calcinations at 500 ◦C for 3 h in a furnace.

2.2 Characterization techniques

The X-ray diffraction (XRD) analysis was examined to assess the crystalline phase of the $ZnFe_2O_4$ nanoparticles utilizing an instrument BRUKER USA D8 Advance, Davinci with CuKα radiation (λ = 1.54060 Å), operating at 40 kV and 30 mA. The characterization purposes, a scanning electron microscope (SEM) with EDX system from OXFORD Instrument have been performed Sigma 300 model was utilized after sputtering the sample and high-resolution transmission electron microscope, specifically the Jeol/JEM 2100, was utilized. Fourier transform infrared (FTIR) spectroscopy was performed using Purkin Elmer model Spectrum Two. The degradation behaviour of the synthesized sample was assessed using a thermal gravimetric and differential thermal analysis (TG/DTA) conducted with a NETZSCH-STA 449 F3 JUPITER instrument. To assess the electrochemical properties, cyclic voltammetry (CV) was performed using a Versa STAT MC model.

3. RESULTS AND DISCUSSION

3.1 XRD analysis

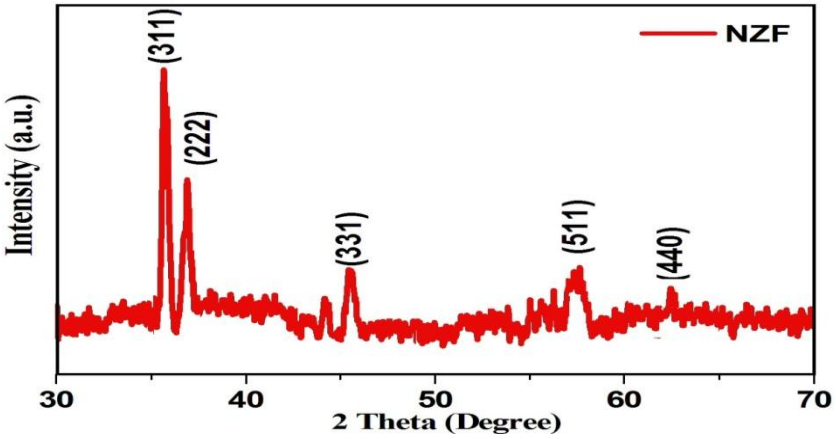

Fig. 1 X-ray diffraction patterns of Ni doped $ZnFe_2O_4$ nanoparticles

In order to investigate the crystal structure of the obtained powder material XRD analysis was performed and the resultant pattern of the as-prepared Ni doped $ZnFe_2O_4$ nanoparticles is presented in Fig. 1. The XRD patterns of the Ni doped $ZnFe_2O_4$ nanoparticles reveal the specific reflections (311), (222), (331), (511) and (440) corresponding to 2-theta angles of 35.32◦, 36.98◦, 41.92◦, 56.86◦, and 62.69◦, respectively, which are match with the characteristic of the Fd-3m cubic spinel structure (JCPDS Card no. 22-1012) [20]. The higher the value of lattice parameter with increase in nickel content is attributed to the replacement of larger Zn^{2+} cation in the interstitial site. The induced strain due to this has been calculated. It is found that strain is maximum for zinc rich sample and decreases as nickel concentration increases. This attributes to the more accommodation of large ionic radii of zinc ion as compared to Ni & Fe in the interstitial site [21]. The average crystallite size (D) of the prepared Ni doped $ZnFe_2O_4$ nanoparticles was determined by using Scherrer's formula [22].

$$D = \frac{0.94\,\lambda}{\beta_D \cos\theta} \qquad \text{(1)}$$

Where β_D is the full width at half maximum (FWHM) of diffracting peak, λ is the wavelength of X-ray (0.1541 nm) and θ is the Bragg's diffraction angle. The crystallite sizes of the sintered Ni doped $ZnFe_2O_4$ nano particles was in the range of 34 nm.

3.2 Structural analysis

Scanning Electron Microscopy (SEM) was utilized to examine the surface morphology and granular microstructure of host zinc ferrites, mainly focusing on the effects of nickel doping. The surface morphology of the synthesized Ni doped $ZnFe_2O_4$ nanoparticles as examined, scanning electron microscope (SEM) and transmission electron microscope (TEM) images are depicted in Fig. 2 (a and b). The synthesized materials show an uneven surface morphology characterized by closely packed tiny blocks and spheres. The environment of SEM micrograms is so typical to identify the shapes of the Ni doped $ZnFe_2O_4$ nanoparticles. From the TEM results (figure 2 (b)), the formation of more small particles on the surface like spherical morphology, distributed uniformly on top of bigger blocks to create a rough surface. The SAED pattern (Fig. 2(c)) reveals the presence of circular rings from the Ni doped $ZnFe_2O_4$ cubic spinel structure and no additional rings are detected. The diffraction rings in the SAED pattern are in good agreement with the standard data (JCPDS Card no. 22-1012)) of Ni doped $ZnFe_2O_4$. From the structural studies, an increase in roughness on the surface of Ni doped $ZnFe_2O_4$ nanoparticles has an impact on the electrochemical properties of the synthesized material since an electrochemical reaction takes place on the surface of the material [3].

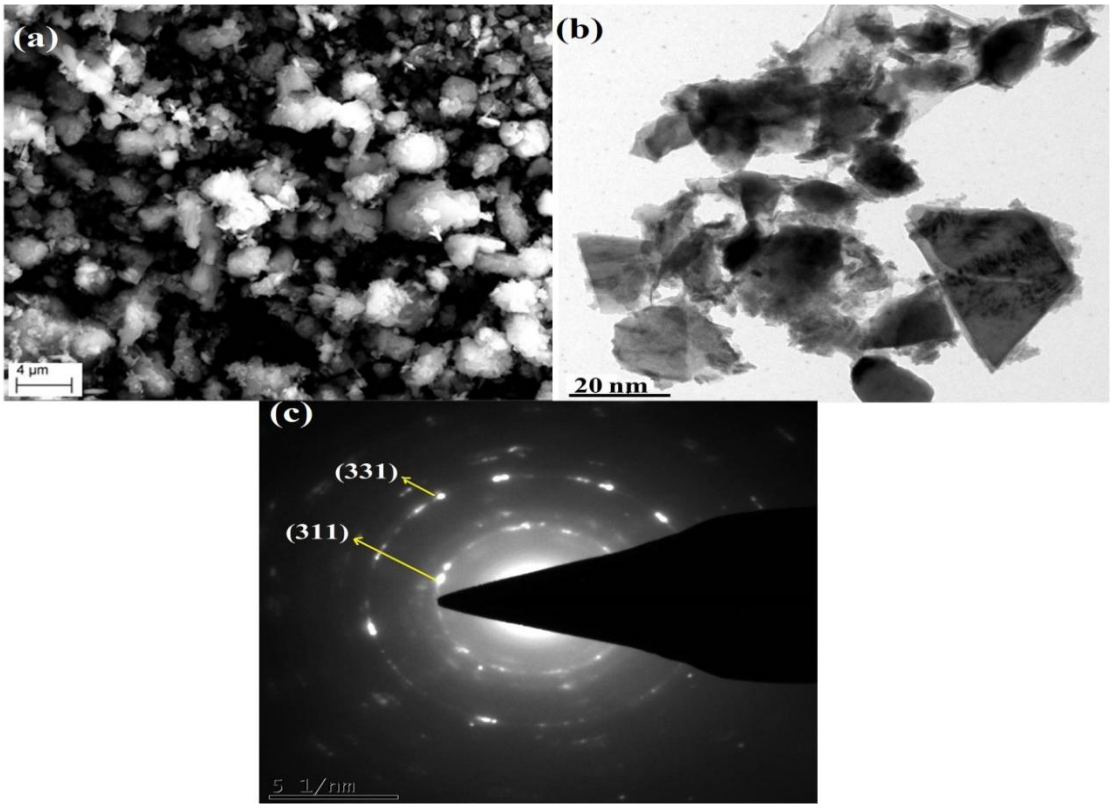

Fig. 2 (a) SEM image, (b) TEM image and (c) SAED pattern of Ni doped $ZnFe_2O_4$ nanoparticles

International Journal of Environmental Sciences
ISSN: 2229-7359
Vol. 11 No. 21s, 2025
https://theaspd.com/index.php

3.3 Elemental composition analysis

Elemental composition analysis of Ni doped $ZnFe_2O_4$ nanoparticles has been studied through the Energy Dispersive X-ray (EDX) spectrum. The characteristic EDX spectra of Ni doped $ZnFe_2O_4$ nanoparticles are shown in Fig. 3, we can clearly observe presence of the constituent elements Fe, Zn, and O in the samples without impurities. The atomic peaks of iron (Fe), zinc (Zn), and oxygen (O) are identified. From the EDX results, Ni, O, Fe and Zn are found to have chemical compositions of 4.20 wt%, 40.71 wt%, 33.47 wt%, and 21.62 wt% in the Ni doped $ZnFe_2O_4$ nanoparticles, respectively. In addition, the atomic percentages (%) for Ni, O, Fe and Zn are found to be 8.11 %, 31.02 %, 40.12 %, and 20.75 %, respectively. Small peaks were also found, which could be due to the impurities from sample holder of the instrument [23]. Fig. 4 (a and b) shows the elemental mapping of the $ZnFe_2O_4$ nanoparticles. From the figure, the signals pertaining to Ni, Zn, Fe, and O have a uniform spatial distribution.

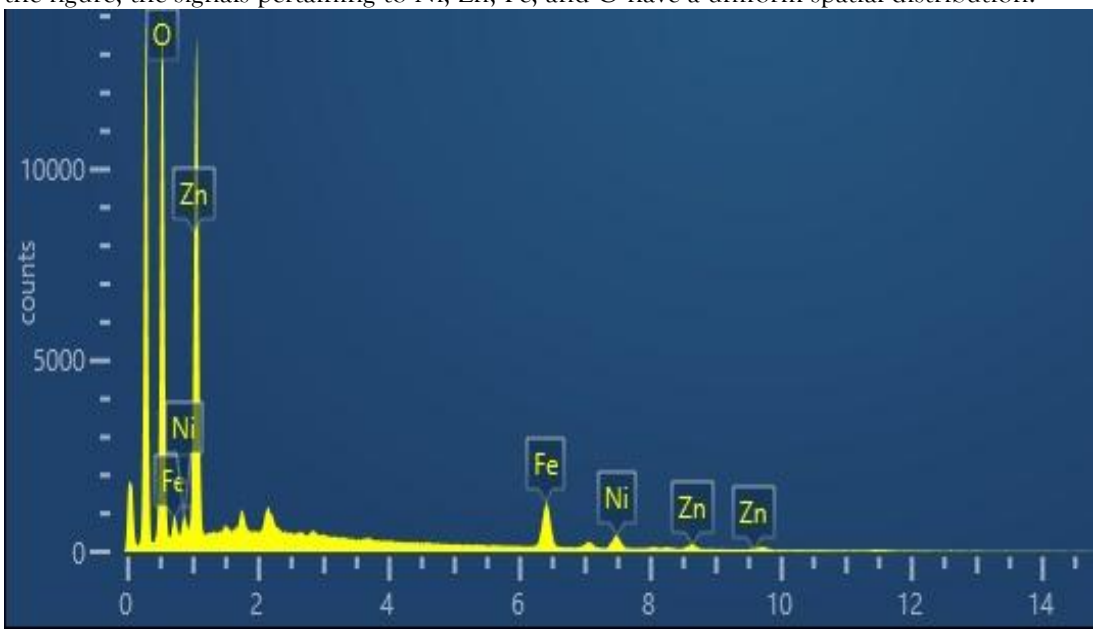

Fig. 3 EDX spectrum of Ni doped $ZnFe_2O_4$ nanoparticles

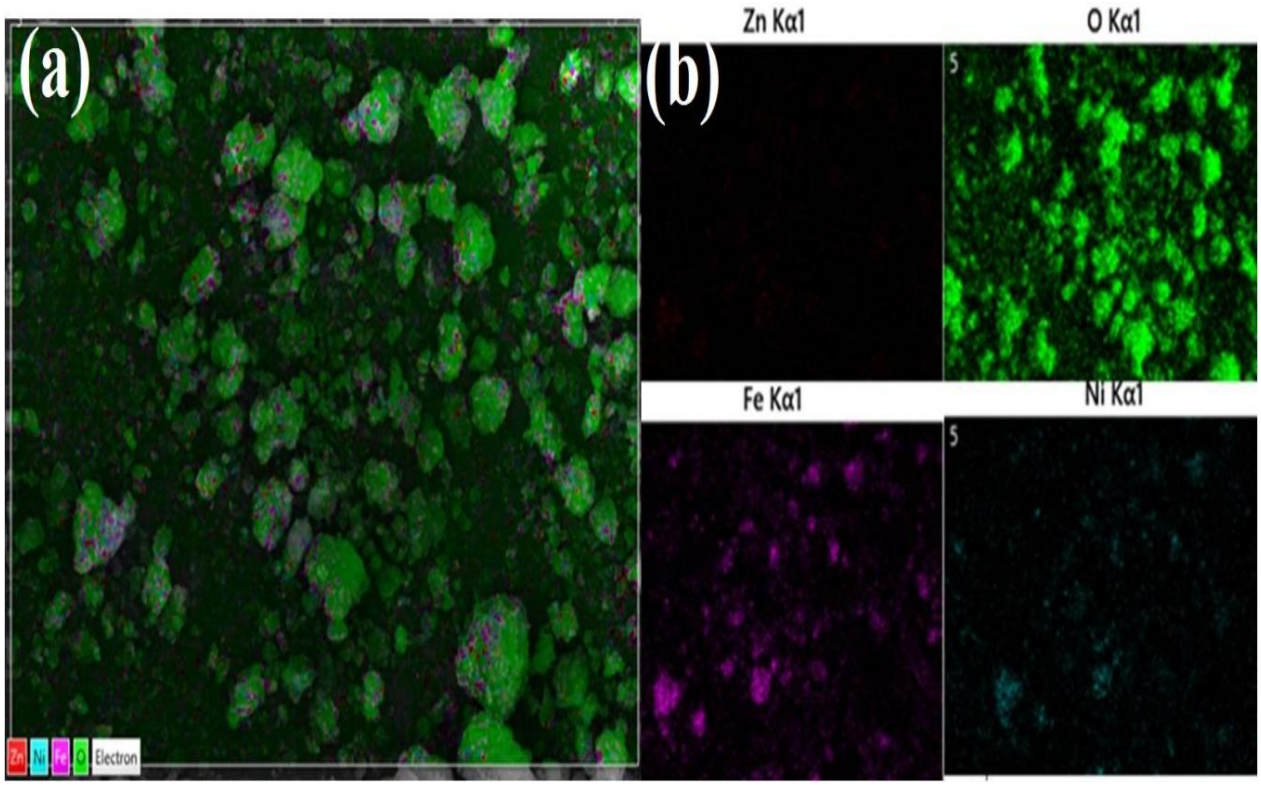

Fig. 4 (a and b) elemental composition images of Ni doped $ZnFe_2O_4$ nanoparticles

3.4 FTIR-spectrum

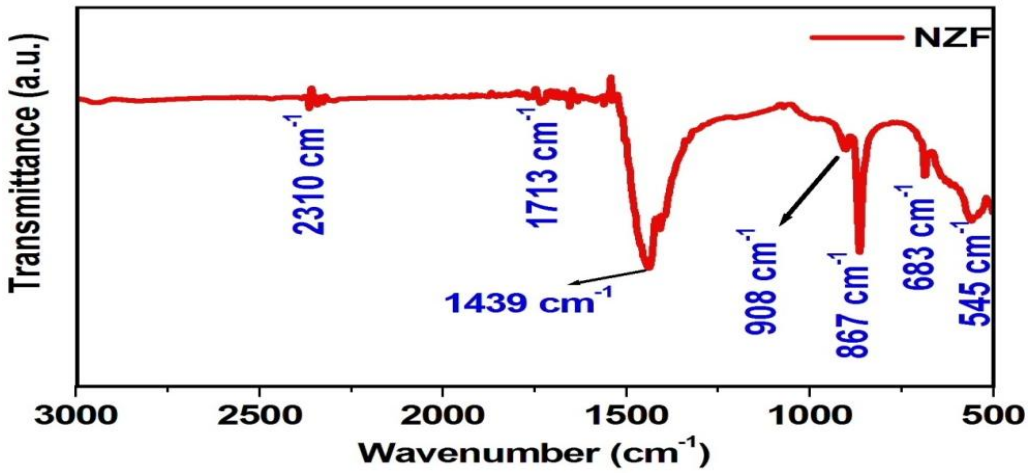

Fig. 5 FTIR spectrums of Ni doped $ZnFe_2O_4$ nanoparticles

FTIR spectrum of Ni doped $ZnFe_2O_4$ nanoparticles are presented in Fig. 5. Vibrations of ions in the crystal lattice are usually recorded in the wavenumber range 3000–500 cm^{-1} at room temperature. From the FTIR spectrum, the highest one (υ1) is generally observed in the range 600–500 cm^{-1}, and it corresponds to intrinsic stretching vibrations of the metal at the tetrahedral site (T_d), M_{tetra} ↔O [18]. Especially, the spectrum showed characteristic peak of tetrahedral and octahedral Fe–O stretching band at 545 cm^{-1} [24]. In literature, the wavenumber 545 cm^{-1} is corresponding to the vibrational mode of the metal oxygen bond (Zn-O-Fe) [25]. The transmittance band at 683 cm^{-1} arises from the lattice vibrations of the oxide ion against relatively heavy metal cations [26]. Additional small bands at 867 cm-1 confirm the successful incorporation of nickel ions in the zinc ferrite. The bands corresponding to 3000 cm^{-1} and 1000 cm^{-1} represent stretching and bending vibrations of H–O–H, which indicates the presence of free or absorbed water in the samples [27]. In addition to these vibrational modes, a broad hump due to bending mode of water at 1713 cm^{-1} are observed in this spectrum. The broadness of stretching mode is attributed to the existence of weak hydrogen bonding [28]. The vibrational band at 2310 cm^{-1} is absorbed water molecules and allocated to the remained free in the Ni doped $ZnFe_2O_4$ during the preparation [29]. Moreover, the peak at 2310 cm^{-1} reveals the O–H stretching vibration of the absorbed water molecule [30]. The symmetric and anti-symmetric stretching modes of carboxylate ions are obtained at 1439 and 1439 cm^{-1}. These peaks indicate the presence of oleic acid in these Ni doped $ZnFe_2O_4$ nanoparticles.

3.5 Thermal analysis (TG/DTA)

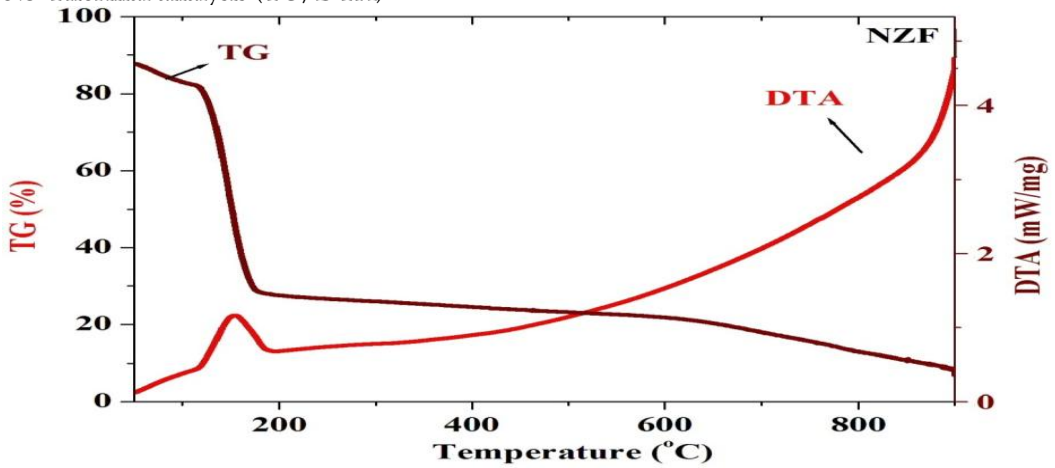

Fig. 6 TG/DTA curve of Ni doped $ZnFe_2O_4$ nanoparticles

Thermal examination of as readied the synthesized Ni doped $ZnFe_2O_4$ nanoparticles was done to explore the development of the spinel ferrite stage. It is recorded in the temperature scope from room temperature to 900°C in nitrogen environment at a warming rate of 10°C/min. The TG and DTA plot for Ni doped $ZnFe_2O_4$ nanoparticles as readied powder is appeared in figure 6. Two major weight losses have been found from TG analysis. The first stage of weight loss is observed at a temperature below 160 °C due to desorption of water. Also, it is seen from TG bend that there is no noteworthy weight reduction after temperature 160 °C which can be ascribed to ferrite stage development. No weight loss is found between

185 °C and 620 °C indicating the formation of Ni doped $ZnFe_2O_4$ nanoparticles. The second weight loss is observed beyond 620 °C due to crystallization of the final product. Additionally, the exothermic peak in DTA curve at 156 °C due to the thermal decomposition of citric acid [31] which is associated in the formation of Ni doped $ZnFe_2O_4$ nanoparticles.

3.6 Cyclic Voltammetry

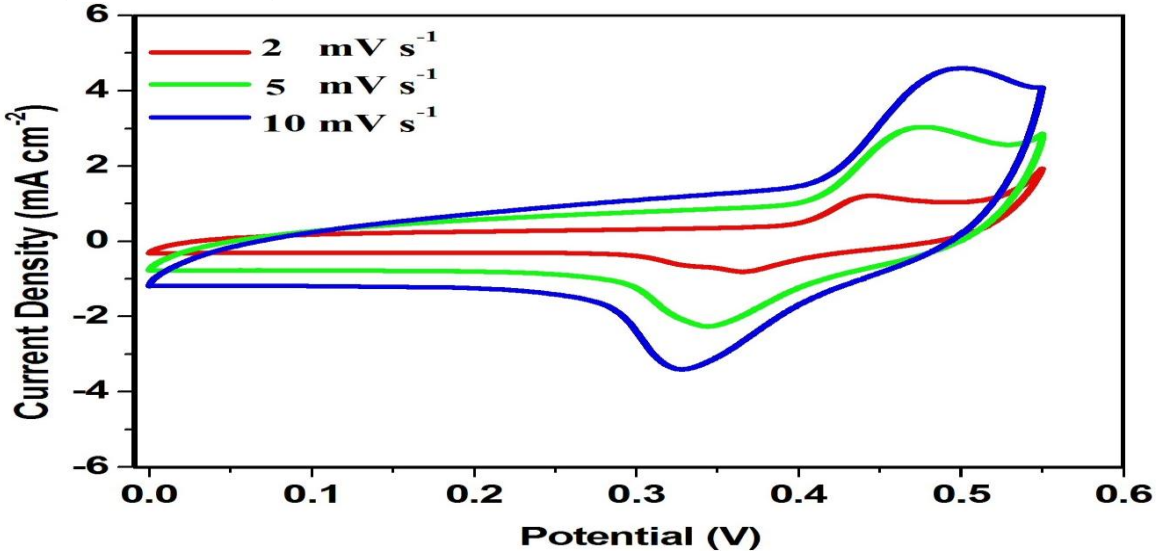

Fig. 7 CV pattern of Ni doped $ZnFe_2O_4$ nanoparticles

Cyclic voltammetry (CV) curves of Ni doped $ZnFe_2O_4$ nanoparticles were performed in at various scan rates (2, 5, and 10 mV s^{-1}) 1 in the 0 V and 0.6 V potential ranges as shown in Fig. 7. As known, the encircled area of CV curves is proportional to the specific capacitance of the electrodes [17]. The CV curves display almost rectangular shape and indicative of well-defined capacitive behavior at low scan rates [32]. In the CV curve of Ni doped $ZnFe_2O_4$ nanoparticles, which underwent annealing at 500 °C, reveal a pseudo-capacitive behavior, as evidenced by changes in the CV patterns with increasing scan rate. This indicates the presence of pseudo-capacitive processes within the system, indicating a dynamic capacitive response influenced by the scan rate. Moreover, when the scan rate increases, oxidation peaks generally shift to higher potentials, and reduction peaks shift to lower potentials. This shift is related to the kinetics of the electrochemical reactions and the ability of the system to reach equilibrium during the potential scan [29]. The CV patterns of the Ni doped $ZnFe_2O_4$ nanoparticles are exhibiting almost symmetrical CVs with small redox peaks indicates pseudo-capacitive characteristics. These curves, typically exhibiting a distorted, non-rectangular shape, indicate the presence of both surface-controlled and diffusion-controlled kinetics, which are property of pseudo-capacitive materials [33]. The shapes of CV curves persist in proportionally unchanged suggests satisfactory electrochemical reversibility. This means the electrochemical response can readily precedes both oxidation and reduction without significant barrier, which lead to stable and expected behavior in the CV [34]. The CV curves showed a prominent oxidation and reduction peak even at higher scan rates, reported by P. Ramadevi et al. [35]. The specific capacitances (C_s) value of the synthesized Ni doped $ZnFe_2O_4$ electrode was calculated by using the following equation [36]

$$Cs = \frac{Q}{\Delta v.m} \qquad \text{..... (2)}$$

For every cyclic voltammetry (CV) scan, Q represents the anodic and cathodic charges, Cs is the specific capacitance, Δv is the scan rate (mV s^{-1}), and m is the mass of the active electrode material (mg). CV measurements were carried out in the possible range of 0.0 to 0.6 V.

The virtually rectangular CV profile of Ni-doped $ZnFeO_4$ suggests faradaic redox activities at the active electrode surface in conjunction with dominating capacitive behaviour. Its pseudocapacitive character is further supported by the existence of two separate redox maxima. Both the oxidation and reduction peak current densities rise proportionately as the scan rate rises from low to high values (Fig. 9), with minor peak changes that indicate quick and reversible redox processes at the electrode surface [37]. Interestingly,

even at a comparatively high scan rate of 10 mV s^{-1}, the CV curves maintain their shape without undergoing considerable distortion, indicating exceptional electrochemical reversibility.

One important finding is that the specific capacitance is at its highest at the lowest scan rate, suggesting that slower scans provide electrolyte ions enough time to reach the porous electrode's inner and outer surfaces [38]. Ion transport is mostly restricted to the outer surface at higher scan speeds, which leads to less efficient use of the active sites. Ni-doped $ZnFeO_4$ has a high mesoporosity, which increases the accessible surface area and facilitates better charge storage performance [39].

Due to the pseudocapacitive structure of the material, the faradaic redox contributions predominate in the charge storage process, which also includes electric double-layer capacitance. The electrode shows the maximum double-layer capacitance at a scan rate of 2 mV s^{-1}, demonstrating effective charge carrier transport and electron–hole separation at the electrode–electrolyte interface. 254 F g^{-1}, 186 F g^{-1}, and 121 F g^{-1} are the specific capacitance values for scan rates of 2, 5, and 10 mV s^{-1}, respectively. This pattern shows that increased capacitance results from lower scan rates, which is beneficial for high-performance supercapacitor applications.

4. CONCLUSION

In summary, Ni-doped $ZnFe_2O_4$ nanoparticles were prepared by low-cost co- precipitation method. The effects of Ni doping on the Structural, compositional, thermal and electrochemical properties of Ni-doped $ZnFe_2O_4$ were investigated. XRD study confirms that the synthesized Ni doped $ZnFe_2O_4$ nanoparticles were single-phase cubic spinel structures and crystallite size range around 34 nm. TEM results were well matched with the crystallite sizes obtained from the XRD data. FTIR results of Ni doped $ZnFe_2O_4$ nanoparticles was confirmed the phase pure with cubic structure. EDX spectrum confirmed the elemental composition of Ni, Fe, Zn and O in the Ni doped $ZnFe_2O_4$ nanoparticles. Thermo-gravimetric and differential thermal analysis (TG/DTA) method was used to confirm the formation of Ni doped $ZnFe_2O_4$ nanoparticles. From the CV analysis, higher capacitance value observed for the scanning rate 2 mV/s. The electrochemical result reflecting the Ni doped $ZnFe_2O_4$ nanoparticles can make it be of great promise in the supercapacitor application.

REFERENCES

1.P. B. Kharat, S. B. Somvanshi and E. A. Dawi, Exploring the electrochemical performance of nickel-zinc ferrite nanoparticles for supercapacitor applications, Journal of Material Science: Materials in Electronics, 35 (2024) 606-614.
2.A. Chouchaine, S. Kouass, F. Touati, N. Amdouni and H. Dhaouadi, Fe3O4 nanomaterials: synthesis, optical and electrochemical properties, Journal of the Australian Ceramic Society, 57 (2021) 469–477.
3.N. Masunga, O. J. Fakayode, B. B. Mamba and V. S. Vallabhapurapu, through rare-earth doping, special attention was paid to improving the photo-electrochemical, optical, magnetic, and structural properties of zinc ferrite, Inorganic Chemistry Communications, 170 (2024) 113406-113414.
4.C.V.G. Reddy, S.V. Manorama, V.J. Rao, Semiconducting gas sensor for chlorine based on inverse spinel nickel ferrite, Sensor. Actuator. B Chem. 55 (1999) 90–95.
5.P. Lavela and J. L. Tirado, CoFe2O4 and NiFe2O4 synthesized by sol–gel procedures for their use as anode materials for Li ion batteries, Journal of power sources, 172 (2007) 379- 387.
6.M. E. C. Ferreira, E. G. Bernardino, M. A. S. D. de Barros, R. Bergamasco, N. U. Yamaguchi, An overview of nanostructured manganese ferrite as a promising visible-light-driven photocatalyst for wastewater remediation, Journal of Water Process Engineering, 54 (2023) 104049-104016.
7.H. Ma, C. Liu, A mini-review of ferrites-based photocatalyst on application of hydrogen production, Front. Energy 15 (2021) 621–630, https://doi.org/10.1007/ S11708-021-0761-0/METRICS.
8.N. Masunga, O.K. Mmelesi, K.K. Kefeni, B.B. Mamba, Recent advances in copper ferrite nanoparticles and nanocomposites synthesis, magnetic properties and application in water treatment: review, J. Environ. Chem. Eng. 7 (2019) 103179,
9.J. Garg, M.N. Chiu, S. Krishnan, R. Kumar, M. Rifah, P. Ahlawat, N.K. Jha, K. K. Kesari, J. Ruokolainen, P.K. Gupta, Emerging trends in zinc ferrite nanoparticles for biomedical and environmental applications, Appl. Biochem. Biotechnol. 196 (2) (2023) 1008–1043.
10. S. N. Pund, P.A. Nagwade, A.V. Nagawade, S.R. Thopate, A.V. Bagade, Preparation techniques for zinc ferrites and their applications: a review, Mater. Today Proc. 60 (2022) 2194–2208.
11. A. Arimi, L. Megatif, L.I. Granone, R. Dillert and D.W. Bahnemann, Visible-light photocatalytic activity of zinc ferrites, Journal of Photochemistry and Photobiology, 366 (2018) 118–126.
12. J. Zhu, Y. Zhu, Z. Chen, S. Wu, X. Fang, Y. Yao, Progress in the preparation and modification of zinc ferrites used for the photocatalytic degradation of organic pollutants, International Journal of Environmental Research in Public Health, 19 (2022) 10710-10719.
13. C. Liu, F. Li, L. P. Ma and H. M. Cheng, Advanced materials for energy storage, Advance Materials, 22 (2010) 28–62.

14. S. Nadaf, B. Chethan, K.M. Swathi, S. S. Laxmeshwar, J. Angadi, K. Manjunatha, M. Vandana, Synthesis, characterization and application of rare earth (Lu3+) doped zinc ferrites in carbon monoxide gas sensing and supercapacitors, Ceramics International, 50 (2024) 23208-23221.
15. S. S. Raut, and B. R. Sankapal, First report on synthesis of ZnFe2O4 thin film using successive ionic layer adsorption and reaction: approach towards solid-state symmetric supercapacitor device. Electrochim. Acta 198, 203–211 (2016).
16. M. Zhu, Facile solvothermal synthesis of porous ZnFe2O4microspheres for capacitive pseudocapacitors. RSC Adv. 5, 39270–39277 (2015).
17. L. Li, H. Bi, S. Gai, F. He, P. Gao, Y. Dai, X. Zhang, D. Yang, M. Zhang and P. Yang, Uniformly Dispersed ZnFe2O4 Nanoparticles on Nitrogen Modified Graphene for High Performance Supercapacitor as Electrode, Scientific Reports, 7 (2016) 43116-43121.
18. M. Sertkol, Y. Koseoglu, A. Baykal, H. Kavas, A. Bozkurt and M. S. Toprak, Microwave synthesis and characterization of Zn-doped nickel ferrite nanoparticles, Journal of Alloys and Compounds, 486 (2009) 325–329.
19. V.D. Kapse, S.A. Ghosh, F.C. Raghuwanshi, S.D. Kapse, U.S. Khandekar, Nanocrystalline Ni0.6Zn0.4Fe2O4: a novel semiconducting material for ethanol detection, Talanta, 78 (2009) 19–25.
20. W. Konicki, D. Siber and U. Narkiewicz, Removal of Rhodamine B from aqueous solution by ZnFe2O4 nanocomposite with magnetic separation performance, Polish Journal of Chemical Technology, 19 (2017) 65-74.
21. A. Kumar, Annveer, M. Arora, M. S. Yadav and R. P. Pant, Induced size effect on Ni doped Nickel Zinc Ferrite Nanoparticles, Physics Procedia, 9 (2010) 20–23.
22. J. Samuel, T. S. F. Rajesh, C. S. Biju, S. S. J. Dhas and S. Usharani, Synthesis, structural, photoluminescence, ultraviolet blocking and antibacterial performances of Ba-doped ZnO nanostructures, Results in Optics, 12 (2023) 100482-100489.
23. J. Samuel, J. E. shaji, S. S. J. Dhas, S. Suresh, V. S. Vinita and C.S.Biju, UV-blocking performance and antibacterial activity of Cd, Ba co-doped ZnO nanomaterials prepared by a facile wet chemical method, Surface and Interface Analysis, 1 (2023) 1-14.
24. G. S. Shahane, A. Kumar, M. Arora, R. P. Pant and K. Lal, Synthesis and characterization of Ni–Zn ferrite nanoparticles, Journal of Magnetism and Magnetic Materials, 322 (2010) 1015–1019.
25. V. A. Fabiani , H. Aldila, Anggraeni and Nuraini, Green synthesis and characterization of Zinc Ferrite (ZnFe2O4) nanocomposite via Tristaniopsis merguensis Griff. natural extract, Earth and Environmental Science, 599 (2020) 012066-012071.
26. A. Manohar, C. Krishnamoorthi, K. C. B. Naidu and C. Pavithra, Dielectric, magnetic hyperthermia, and photocatalytic properties of ZnFe2O4 nanoparticles synthesized by solvothermal refux method, Applied Physics A, 125 (2019) 477-484.
27. M. Deepty, C. Srinivasa, E. R. Kumar, N. K. Mohan, C. L. Prajapate , T. V. Chandrasekhar Raoe , S. S. Meena , A. K. Verma and D. L. Sastry, XRD, EDX, FTIR and ESR spectroscopic studies of co-precipitated Mn–substituted Zn–ferrite nanoparticles, Ceramics International, 45 (2019) 8037–8044.
28. M. G. Naseri, M. H. M. Ara, E. B. Saion and A. H. Shaar, Super-paramagnetic magnesium ferrite nanoparticles fabricated by a simple, thermal-treatment method, J. Magnetism and Magnetic Materials, 350 (2014) 141–147.
29. L. A. Kafshgari, M. Ghorbani and A. Azizi, Synthesis and characterization of manganese ferrite nanostructure by co-precipitation, sol-gel, and hydrothermal methods, Particulate Science and Technology, 37 (2018) 904–910.
30. M. M. N. Ansari, S. Khan and N. Ahmad, Effect of R3+ (R= Pr, Nd, Eu and Gd) substitution on the structural, electrical, magnetic and optical properties of Mn-ferrite nanoparticles, Journal of Magnetism and Magnetic Materials, 465 (2018) 81–87.
31. P. Sivagurunathan and K. Sathiyamurthy, Effect of Temperatures on Structural, Morphological and Magnetic Properties of Zinc Ferrite Nanoparticles, Canadian Chemical Transactions, 4 (2016) 244-254.
32. D. Abisha, S. R. Gibin, V. K. PremKumar and A. Mariappan, Improved supercapacitor application of manganese ferrite nanoparticles via co-precipitation technique, Heliyon, 9 (2023) 21120-21131.
33. N. Maile, S. K. Shinde, S. S. Patil, D. Y. Kim, A. V. Fulari, D. S. Lee and V. J. Fulari, Capacitive property studies of electrochemically synthesized Co_3O_4 and Mn_3O_4 on inexpensive stainless steel current collector for supercapacitor application, Ceramics International, 46 (2020) 14640-14649.
34. G. Nabi, K. N. Riaz , M. Nazir, W. Raza, M. B. Tahir, M. Rafique, N. Malik, A. Siddiqa, S. S. Ali Gillani, M. Rizwan, M. Shakil and M. Tanveer, Cogent synergic effect of TiS2/g-C3N4 composite with enhanced electrochemical performance for supercapacitor. Ceramics International, 46 (2020) 27601-27607.
35. P. Ramadevi, F. Kousi, A. Sangeetha, M. S. Mano Gibson, R. Shanmugavadivu, Structural and electrochemical investigation on pure and nickel doped cobalt ferrite nanoparticles for supercapacitor application, Materials Today: Proceedings, 33 (2020) 2238-2243.
36. S. C. Pang, B. H. Wee and S. F. Chin, The capacitive behaviors of manganese dioxide thin-film electrochemical capacitor prototypes, International Journal of Electrochemistry, 2011 (2011).
37. K. Sathishkumar, N. Shanmugam, N. Kannadasan, S. Cholan and G. Viruthagiri, Opto, magnetic and electrochemical characterization of Ni1— xCoxO nanocrystals, Journal of Materials Science: Materials in Electronics, 26 (2015) 1881–1889.
38. D. Toloman, A. Gungor, A. Popa, M. Stefan , S. Macavei, L. B. Tudoran, A. Varada, I. Deniz Yildirim, R. Suciu, I. Nesterovschi, M. Mihet, E. Erdem and A. M. Rostas, Morphological impact on the supercapacitive performance of nanostructured ZnO electrodes, Ceramics International, 51 (2025) 353–365.
39. N. Kitchamsetti, Y. R. Ma, P. M. Shirage and R. S. Devan, Mesoporous perovskite of interlocked nickel titanate nanoparticles for efficient electrochemical supercapacitor electrode, Journal of Alloys and Compounds, 833 (2020) 155134-155147.